Supporting Information for

Bulk-Interface Engineering of CoO_x/SCN Heterostructure for Synergistically Enhanced Photocatalytic Degradation of Imidacloprid Insecticide

Guangxue Pan [1, ‡], Yan, Zhang[1, ‡], Mengmeng Liu [1, ‡], Zhuwei Cao [1, ‡], Yi Zheng, Sheng Ye [1, *]

[1] Agricultural Photocatalysis Laboratory, School of Materials and Chemistry & School of Plant Protection, Anhui Agricultural University, Hefei 230036, China

‡ These authors contributed equally

* Corresponding author

E-mail address: sye503@ahau.edu.cn (S. Ye)

Contents

1. Details of the experiment

1.1. Materials. Melamine (99%), Triolethiocyanic Acid (99%), Cobalt Nitrate Hexahydrate (99%), Sodium Iodate (99%), Dimethyl Sulfoxide (99%), Absolute Ethanol (⩾95%), Imidacloprid (97%), 2, 2, 6, 6-tetramethylpiperidinyl-1-oxide (99%), Methanol (AR), Isopropanol (AR), Potassium dichromate (AR).

1.2. Synthesis Methods. Bulk CN (denoted CN-B) was synthesized via direct calcination of melamine in a muffle furnace at 550 °C for 7 h (Anhui Kemi Instrument Co., Ltd. BFC-1200). For camellia-like CN (denoted CN-C), a thermal polymerization process was implemented by dissolving melamine and cyanuric acid in dimethyl sulfoxide (DMSO), followed by annealing the mixture in the muffle furnace.

The vacuum-dried CN-C heterostructure was homogeneously blended with trithiocyanuric acid through mechanical grinding, followed by controlled thermal treatment in a muffle furnace to synthesize sulfur-doped CN (denoted SCN). Different S-doped samples were prepared by incorporating varying amounts of thiocyanate with concentrations of 1%, 5%, 10%, 15%, and 20%, labeled as SCN-1 to SCN-5, respectively.

The SCN-3 substrate (90 mg) was dispersed in 0.01% $NaIO_3$ solution, followed by addition of 276 μL $Co(NO_3)_2 \cdot 6H_2O$ (6.512 mg mL^{-1}) and light-driven photodeposition (2 h) to obtain the 0.5% CoO_x-loaded heterostructure photocatalyst (designated CoO_x/SCN-3). Gradient CoO_x loading (0.05%-2%) samples were fabricated with corresponding CoO_x/SCN-1 to CoO_x/SCN-5 nomenclature. SCN-3 and CoO_x/SCN-3 are systematically referred to as SCN and CoO_x/SCN following standardized nomenclature.

1.3. Characterization Techniques. The crystallographic phase and structural characteristics of the catalyst were analyzed using X-ray diffraction (XRD). Morphological examination and microstructural characterization were performed using a Hitachi S-4800 field emission scanning electron microscope (SEM) equipped with an energy-dispersive X-ray spectroscopy (EDS) detector, complemented by high-resolution imaging obtained from a JEM-2100F transmission electron microscope (TEM). Chemical bonding states were investigated through Fourier transform infrared (FT-IR) spectroscopy (Nicolet IS50) employing the conventional KBr pellet preparation method. X-ray photoelectron spectroscopy (XPS) was performed using Mg Kα radiation (1253.6 eV) in an ultrahigh vacuum system at the photoemission endstation of the National Synchrotron Radiation Laboratory (NSRL), University of Science and Technology of China (USTC). X-ray near-edge structure (XANES) measurements were used to investigate the effect of C and N atoms in CN using total electron yield. The specific surface area and pore size of four different sample were calculated using BJH and BET analysis using BEL Master7. The CoO_x loading amount was tested using ICP-MS (NexION 2000).

1.4. Density Functional Theory (DFT) Calculations. DFT calculations were carried out using First-Principles Calculations. The generalized gradient approximation (GGA) approach of Perdew-Burke-Ernzerhof (PBE) was employed to calculate the exchange-correlation energy. Effective core potential (ECP) and double numerical polarization (DNP) basis sets were employed to ensure accuracy and efficiency of the calculations. During the geometry optimization process, energy, force, and displacement convergence criteria were set to 1×10^{-4} Ha, 0.03 eV $Å^{-1}$, and 0.005 Å, respectively, while the convergence criterion for the self-consistent field was set to 1×10^{-5} Ha.

1.5. Photoelectrochemical Characterizations and Photocatalytic Performance. The electrochemical impedance spectroscopy (EIS) and transient photocurrent response (TPC) performance of CN-B, CN-C, SCN and CoO_x/SCN was evaluated using a three-electrode configuration in 0.5 M Na_2SO_4 with an electrochemical workstation (Wuhan Corrtest CS310M). The catalyst (50 mg) was added to 100 mL of IMI solution with a concentration of 5 ppm (Beijing Ceaulight CEL-LAB200E7), and the degradation was carried out for 6 h under the irradiation of the full spectrum. The photocatalytic degradation performance of IMI was measured (Beijing CEAuLight Technology Co., Ltd.). For mechanistic studies of pesticide degradation, high-performance liquid chromatography coupled with tandem mass spectrometry (HPLC-MS/MS) was employed to conduct time-dependent qualitative analysis.

1.6 Surface photovoltage. The spatially-resolved surface photovoltage microscope (SPVM) setup was installed in a Kelvin probe force microscopy (KPFM) setup (Bruker Dimension FastScan) consisting of a modified Dimension Icon. Samples were prepared by transferring the particles onto a carbon conductive adhesive. KPFM measurements were conducted in lift mode, where the topography and surface potential signals were acquired sequentially. For surface photovoltage (SPV) measurements, the lift mode with a height of 100 nm was employed. The contact potential difference (CPD), which represents the surface potential, was measured under ambient conditions in amplitude-modulated mode. The CPD is defined as:

$$\mathrm{CPD} = \varphi_{\mathrm{Sample}} - \varphi_{\mathrm{tip}}$$

Where φ represents the potential, and the smaller the measured CPD, the lower the sample potential, and the higher the corresponding work function. The Pt/Ir-coated Sb-doped Si tip (SCM-PIT-V2) was used as a Kelvin tip. A 450 nm LED (2 mW cm–2) almost parallel to the substrate was used to measure the CPD under illumination.

1.7 Safety assessment of daphnia. The safety test of daphnia was conducted in accordance with the standard of GB/T 31270.13-2014 of the People's Republic of China. The river water is collected from the Yuhua pond in Shushan District, Hefei City, Anhui Province. The concentrations of IMI and five different degradation products in the culture flasks were 500 ug/mL. Approximately 30 daphnia were placed in each culture flask.

2. Supporting Images

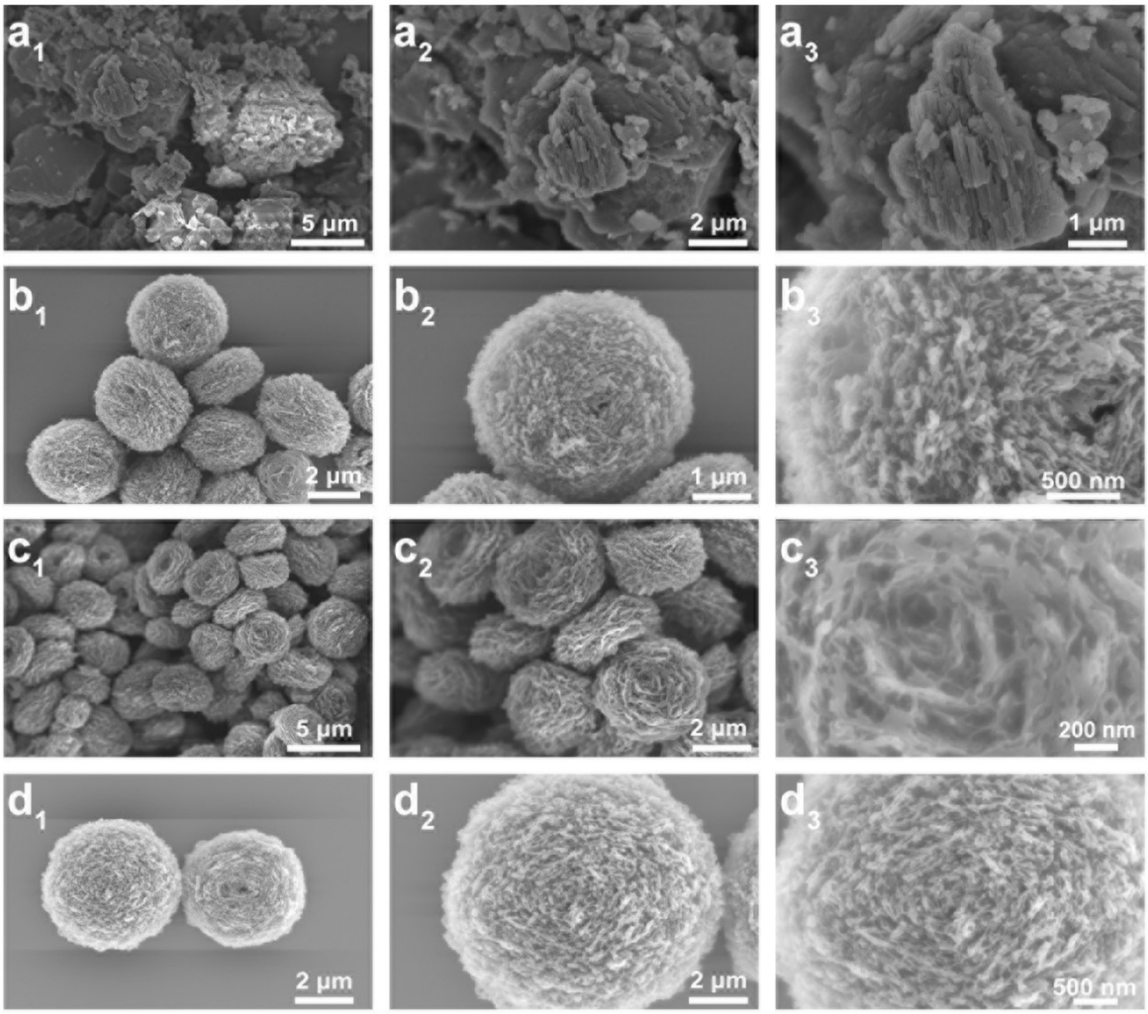

Figure S1. SEM images of (a) CN-B, (b) CN-C, (c) SCN, (d) CoO_x/SCN.

The SEM images of the four different catalysts reveal distinct morphological features. CN-B exhibits a stacked flake-like structure. In contrast, CN-C, SCN, and CoO_x/SCN all show a uniform camellia-like morphology, which are aggregates formed by a network of nanosheets, displaying slight differences in particle size.

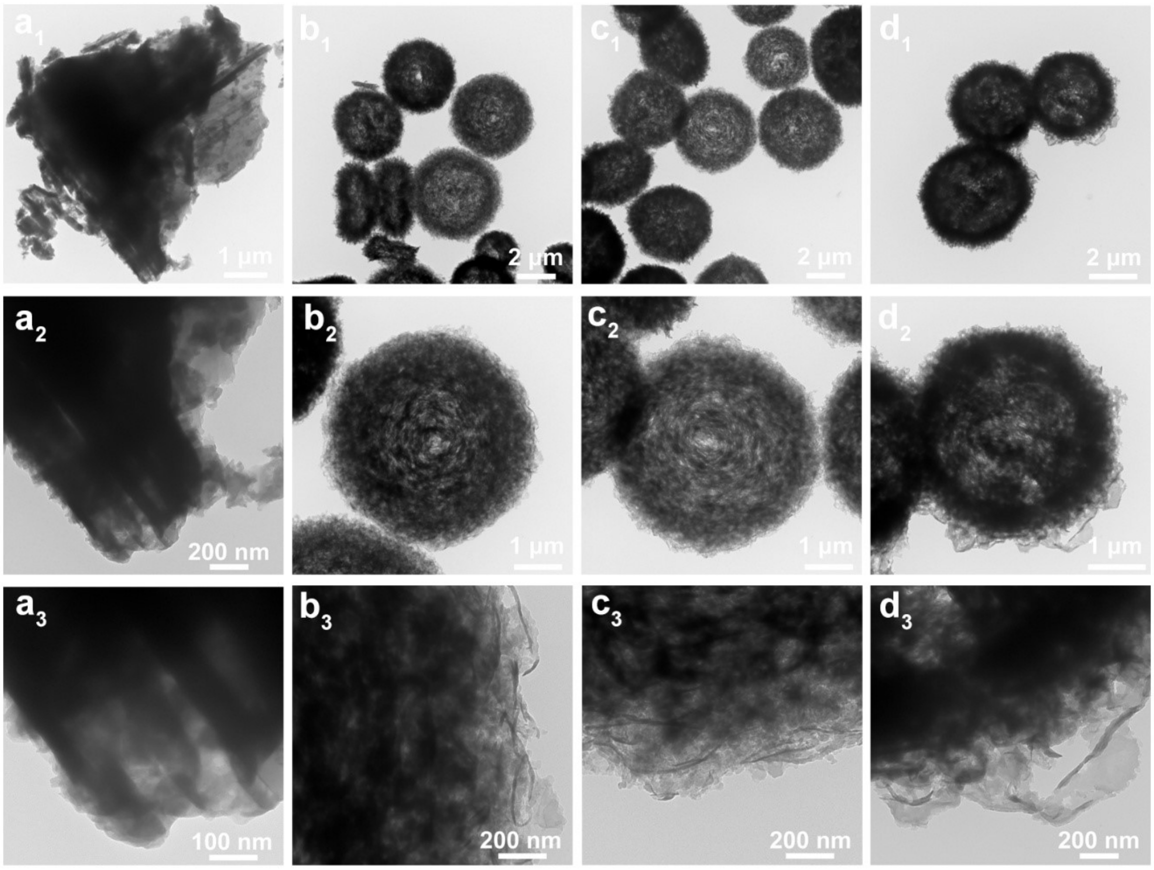

Figure S2. TEM images of (a) CN-B, (b) CN-C, (c) SCN, (d) CoO_x/SCN.

The TEM images of the four different catalysts reveal distinct structural characteristics. CN-B exhibits a stacked nanosheet morphology, with a thick center and thinner edges, where the nanosheet structure is regular at the edges. In contrast, CN-C, SCN, and CoO_x/SCN all display a camellia-like morphology, with relatively large voids. The SCN morphology shows larger voids and a noticeable aggregation center.

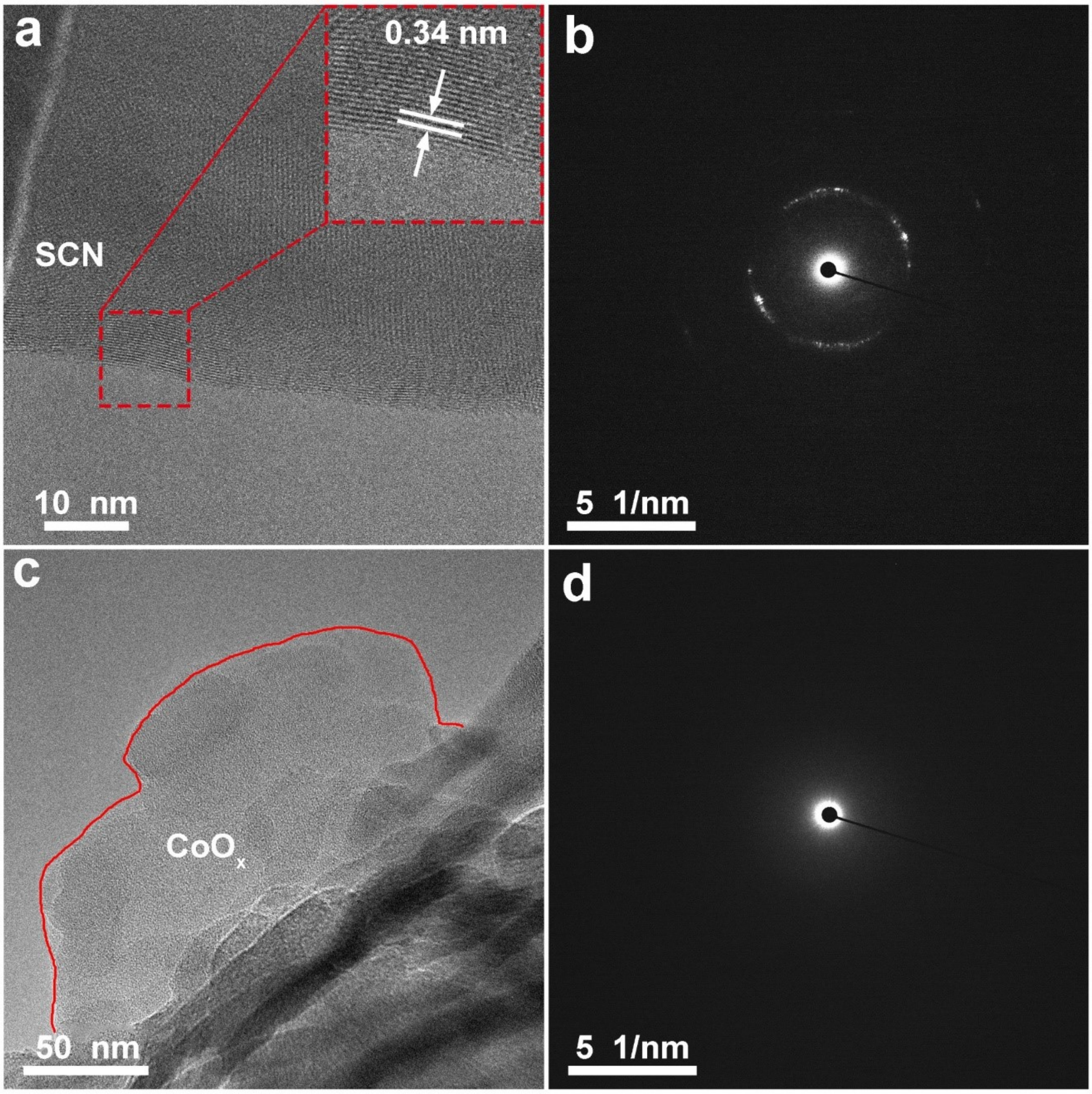

Figure S3. HRTEM images of (a) CN and (c) CoO$_x$, SAED images of (b) CN and (d) CoO$_x$.

Distinct lattice fringes are discernible in the HRTEM image, which demonstrates the well-defined crystalline structure of CN in Figure S3a. The measured lattice spacing of 0.32 nm corresponds to the (002) crystallographic plane of CN. No lattice was observed in Figure S3b, indicating that CoO$_x$ exists in an amorphous form. The selected area electron diffraction (SAED) pattern, as shown in Figure S3b and S3d, displays diffraction ring, indicating the polycrystalline properties of CN and the amorphous nature of CoO$_x$.

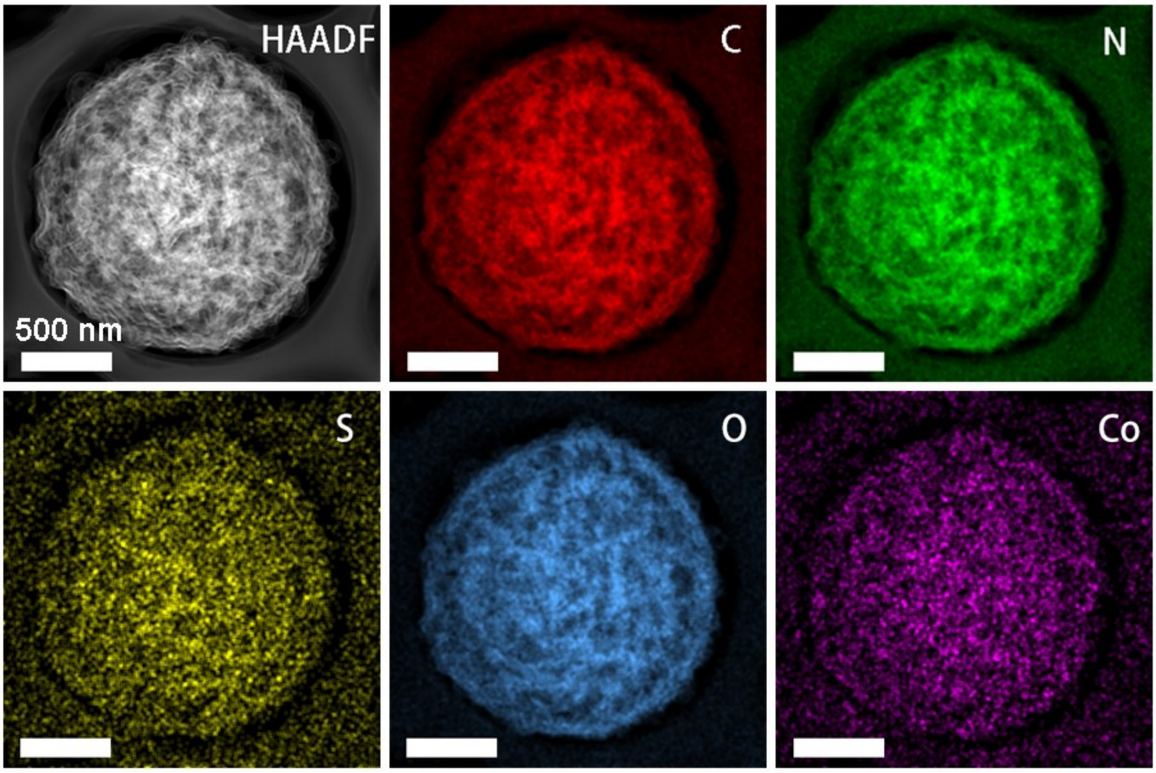

Figure S4. EDS mapping of CoOx/SCN.

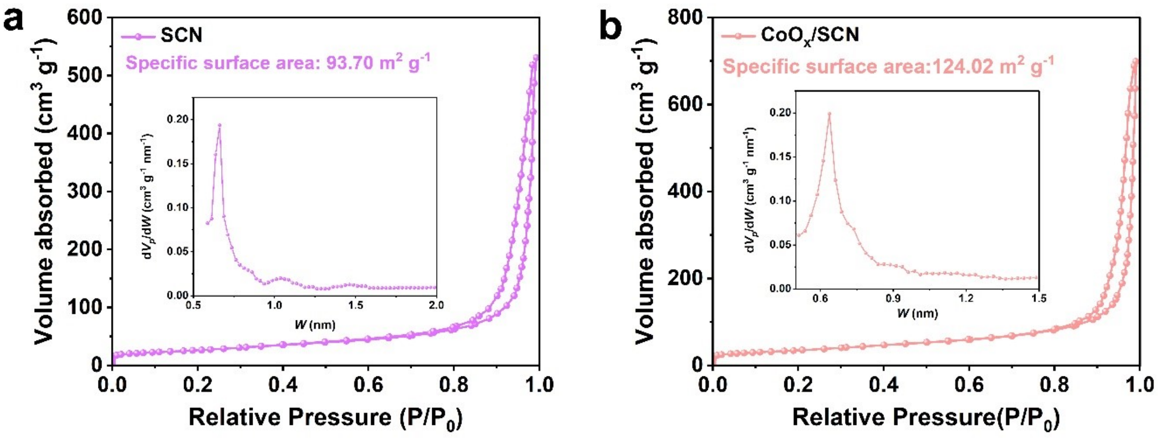

Figure S5. The specific surface area and pore size of (a) SCN and (b) CoO_x/SCN.

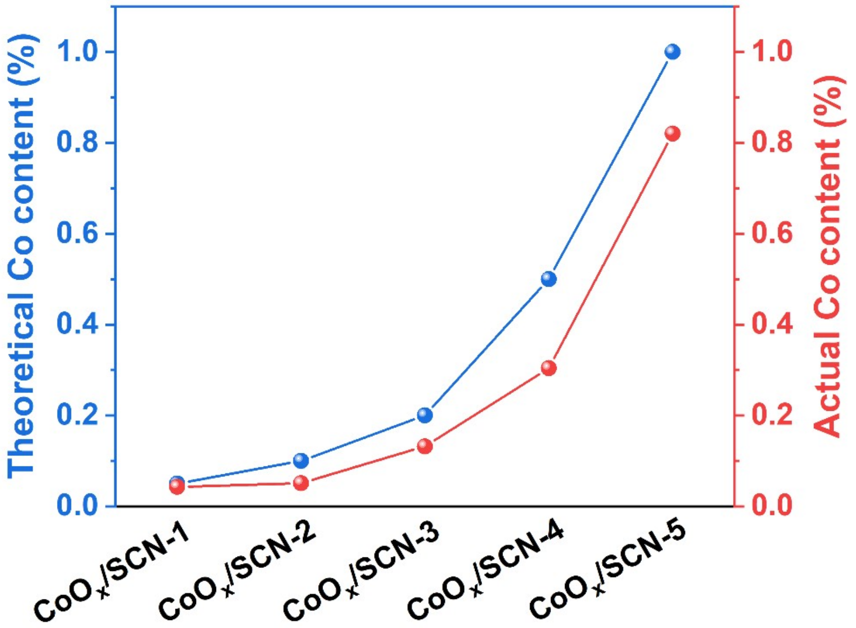

Figure S6. ICP testing of CoO$_x$/SCN with different contents.

ICP analysis was performed to quantify the Co content in the CoO$_x$/SCN heterostructure. The measured Co loading shows good agreement with the theoretical value, confirming the effectiveness of the photodeposition method.

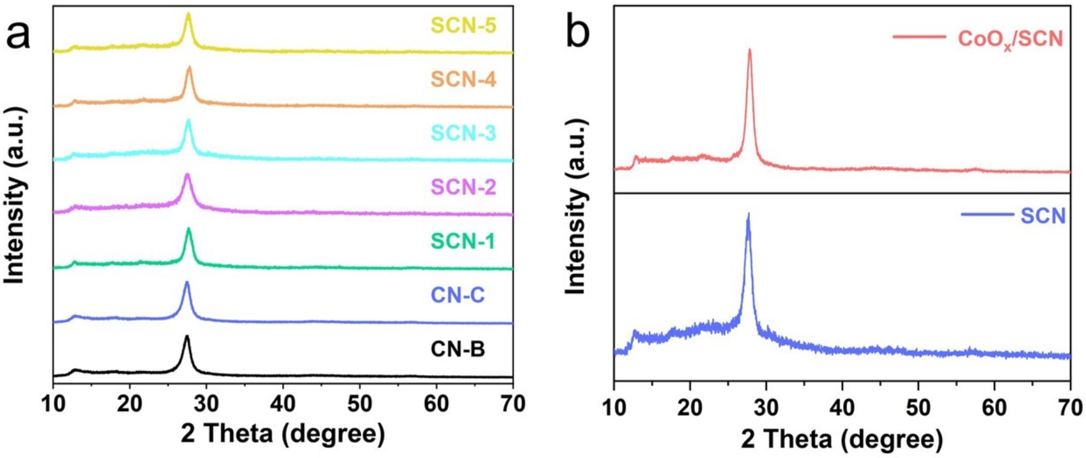

Figure S7. XRD of (a) CN-B, CN-C and SCN with different contents, (b) SCN and CoO_x/SCN.

XRD analysis indicates that the SCN samples do not exhibit any new diffraction peaks and show two major diffraction peaks at 13° and 27.4°, corresponding to the (100) and (002) planes of C_3N_4, respectively. Compared to pure C_3N_4, the diffraction peak around 27.4° of the SCN shows a slight shift, with the degree of shift varying depending on the sulfur doping content. The XRD pattern of CoO_x/SCN-3 shows a reduction in the intensity of the diffraction peaks at 13° and 27°.

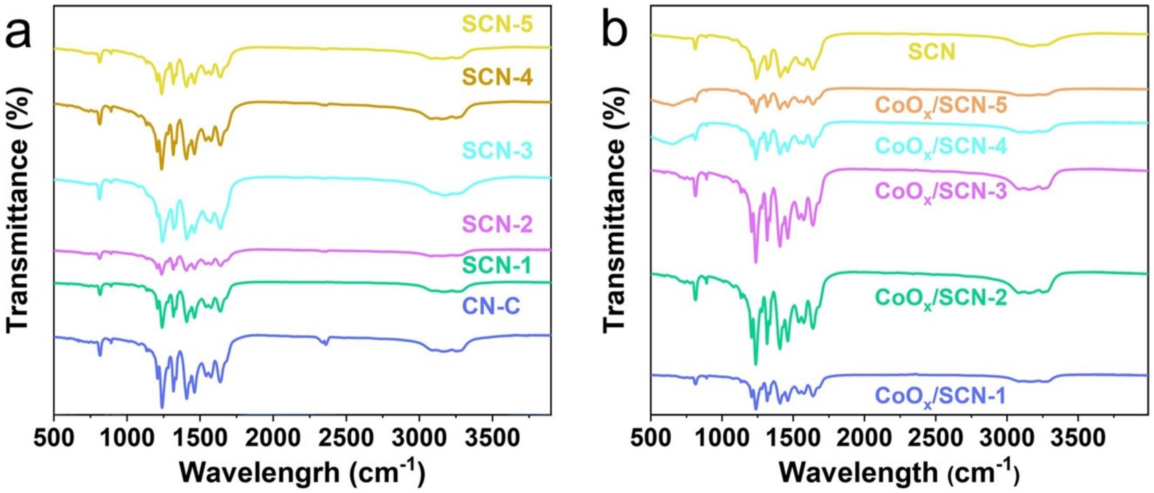

Figure S8. FT-IR of (a) CN and SCN with different contents, (b) SCN and CoO_x/SCN.

In the Fourier transform infrared (FTIR) spectra, several prominent absorption peaks can be observed, reflecting the molecular vibration characteristics of C_3N_4 and its sulfur-doped derivatives. The peak at 802 cm^{-1} is typically associated with the characteristic breathing vibration of the triazine units, indicating the presence of triazine rings in the C_3N_4 structure. The fingerprint region between 1200 and 1600 cm^{-1} is primarily attributed to the stretching vibrations of C-N heterocycles, which is a characteristic feature of C_3N_4. The broad absorption band between 2900 and 3300 cm^{-1} is mainly caused by incompletely condensed amino groups and surface-adsorbed water molecules. This band is particularly intense in the sulfur-doped samples, with significant variations observed depending on the sulfur doping levels. This may be due to the enhanced stretching of the S-N bond induced by sulfur doping.

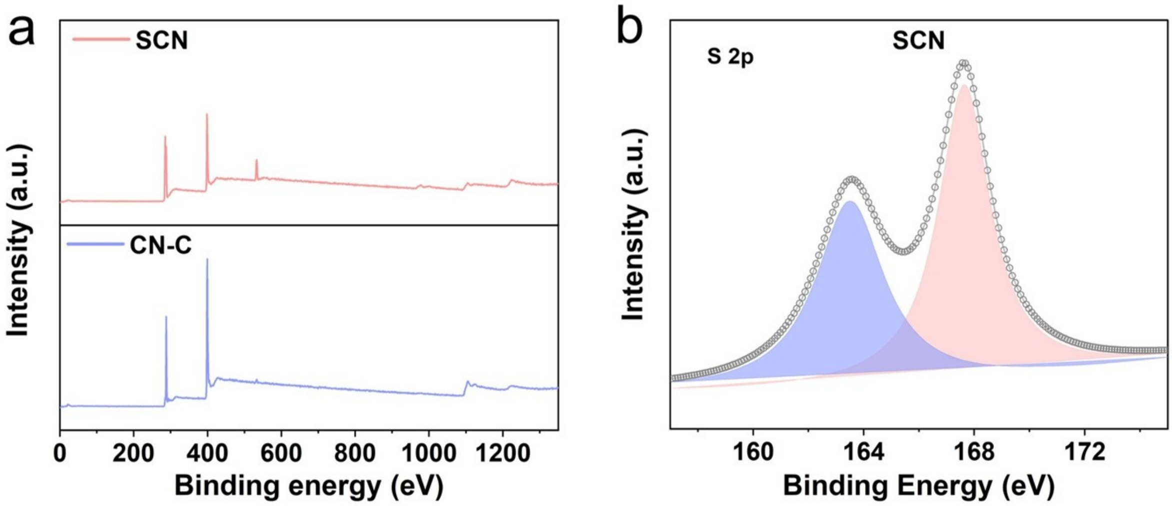

Figure S9. XPS (a) survey of CN-C and SCN, (b) S 2p of SCN.

In the S 2p spectrum, two peaks at 163.5 eV and 167.7 eV are detected, corresponding to the binding energies of S $2p_{3/2}$ and S $2p_{1/2}$, respectively.

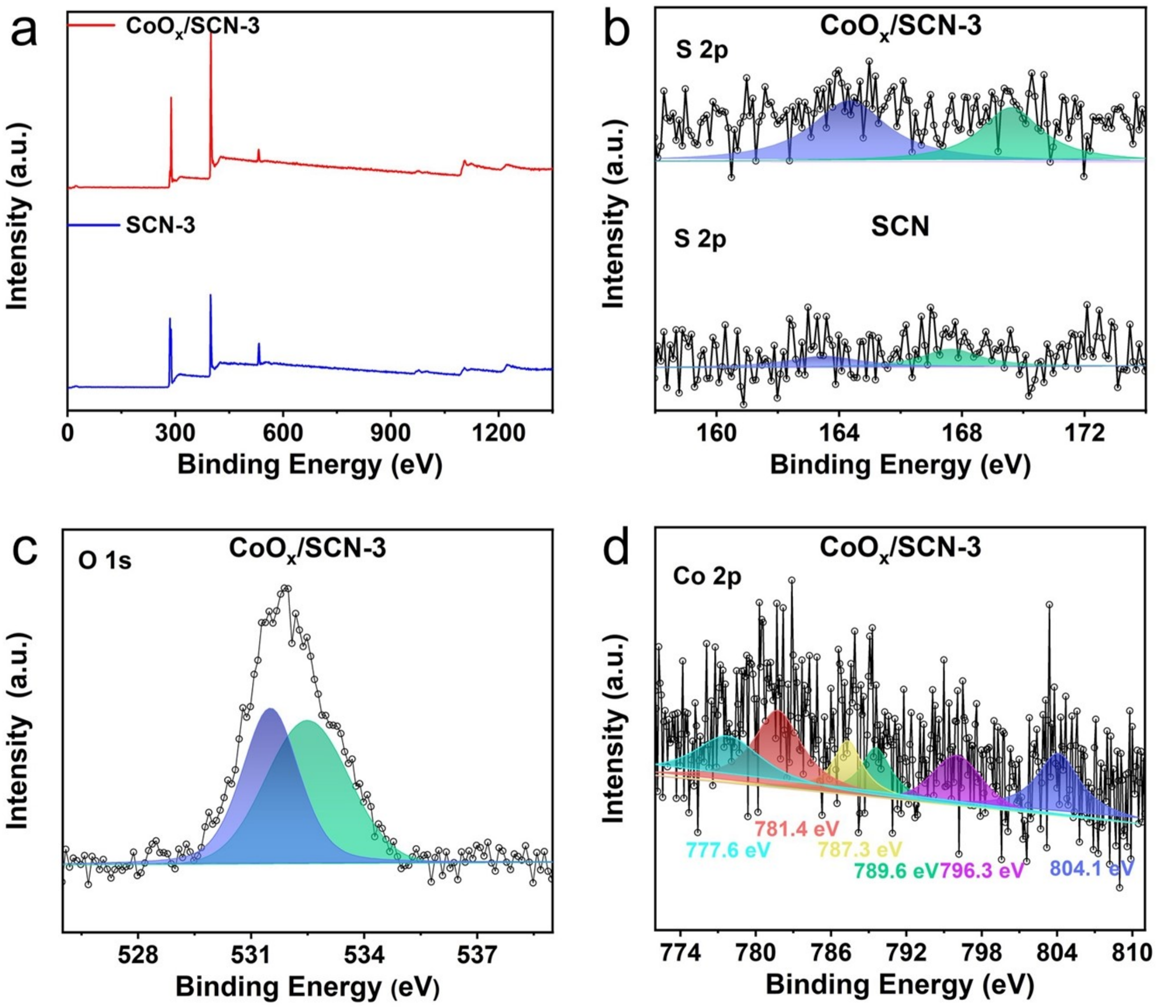

Figure S10. XPS (a) survey, (b) S 2p, (c) O 1s, (d) Co 2p spectrum of CoO$_x$/SCN and SCN.

In the S 2p spectra of CoO$_x$/SCN and SCN, two peaks were observed at 162.3 eV and 167.7 eV. Compared to SCN, these peaks in the CoO$_x$/SCN spectra exhibited a significant right shift and an increase in peak intensity.

The O 1s spectrum of CoO$_x$/SCN shows two peaks at 531.5 eV and 532.6 eV, which are attributed to the binding energies of C=O and C-O bonds, respectively. The Co 2p XPS spectrum of CoO$_x$/SCN-3 exhibits six peaks at 777.6 eV, 781.4 eV, 787.3 eV, 789.6 eV, 796.3 eV, and 804.1 eV. Among these, the peaks at 781.4 eV and 796.3 eV are assigned to Co 2p$_{1/2}$ and Co 2p$_{3/2}$, respectively, corresponding to Co^{3+} and Co^{2+}. Additionally, the peaks at 789.6 eV and 804.1 eV are identified as satellite peaks associated with the Co 2p$_{3/2}$ and Co 2p$_{1/2}$ states.

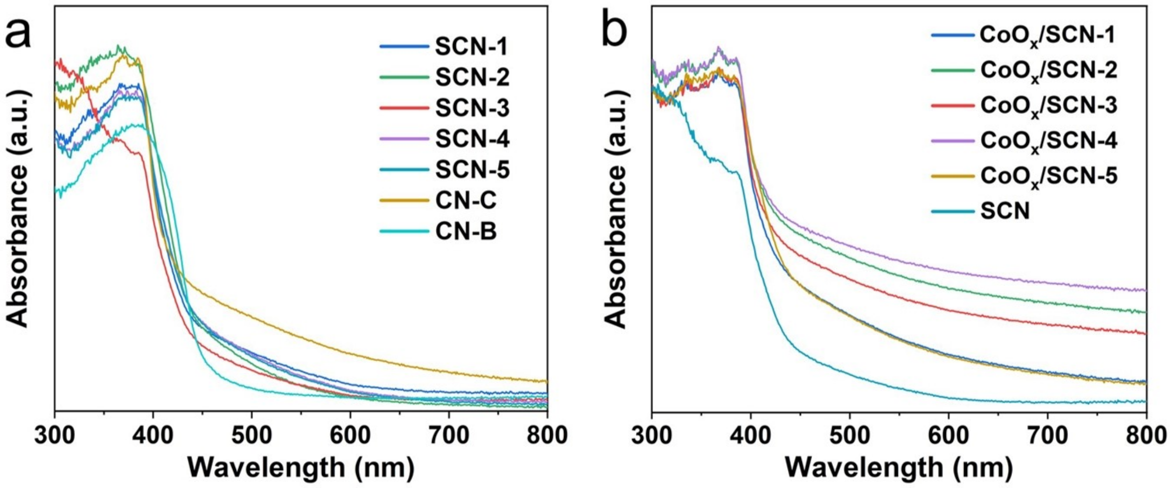

Figure S11. UV-vis of (a) CN-B, CN-C and SCN with different contents, (b) SCN and CoO_x/SCN with different CoO_x loading amounts.

In the UV-vis absorption spectra, distinct differences in absorption values are observed among the samples with varying S doping levels, although the overall variation is not significant. There was no significant change in light absorption after loading the cocatalyst CoO_x.

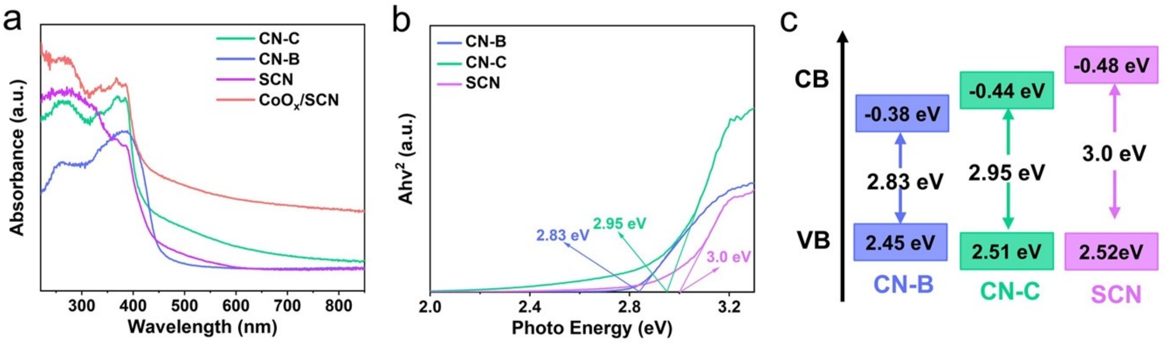

Figure S12. UV-vis of (a) CN-B, CN-C, SCN and CoO$_x$/SCN, (b) energy band gap and (c) band structure of CN-B, CN-C and SCN.

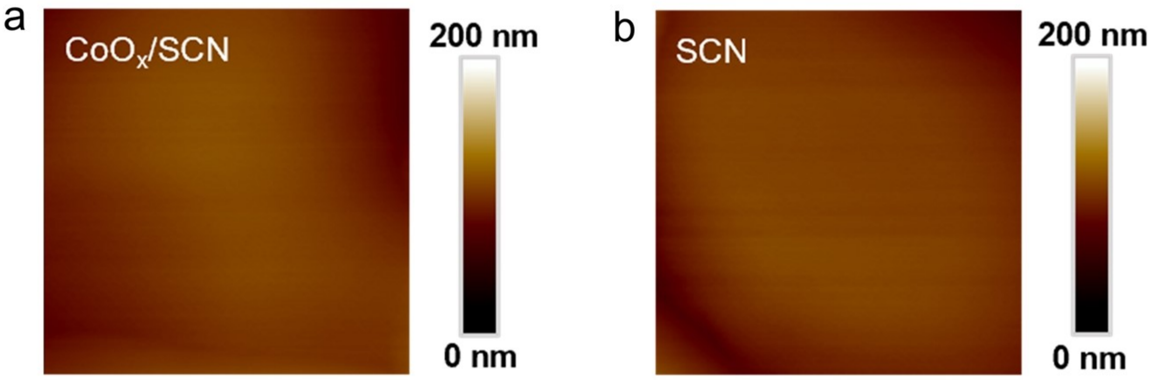

Figure S13. Surface photovoltage images of SCN, CoO$_x$/SCN. (a, b) Topography images, CPD maps.

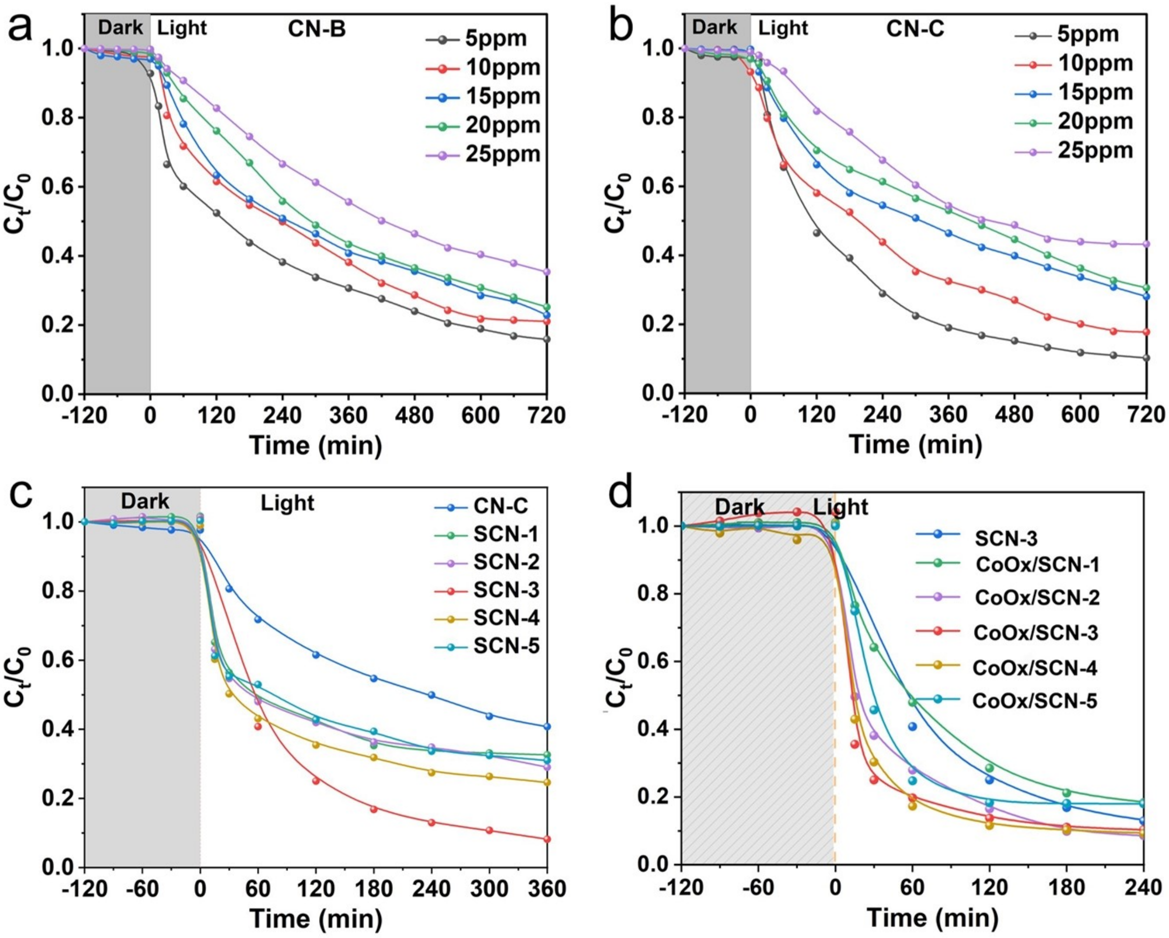

Figure S14. Photocatalytic degradation of imidacloprid by (a) CN-B, (b) CN-C, (c) SCN with different contents, (d) CoO_x/SCN with different contents.

In photocatalytic degradation experiments, CN-B and CN-C were used as photocatalysts in IMI solutions at concentrations of 5, 10, 15, 20, and 25 ppm to evaluate their degradation performance under varying concentrations. As the IMI concentration decreased, the photocatalytic degradation efficiency increased. Following sulfur doping, with a reaction time of 6 hours, all SCN doped samples exhibited higher degradation efficiencies than CN-C. After loading with the CoO_x cocatalyst, approached 90% after 2 hours, indicating that CoO_x/SCN significantly enhanced the photocatalytic degradation efficiency of IMI.

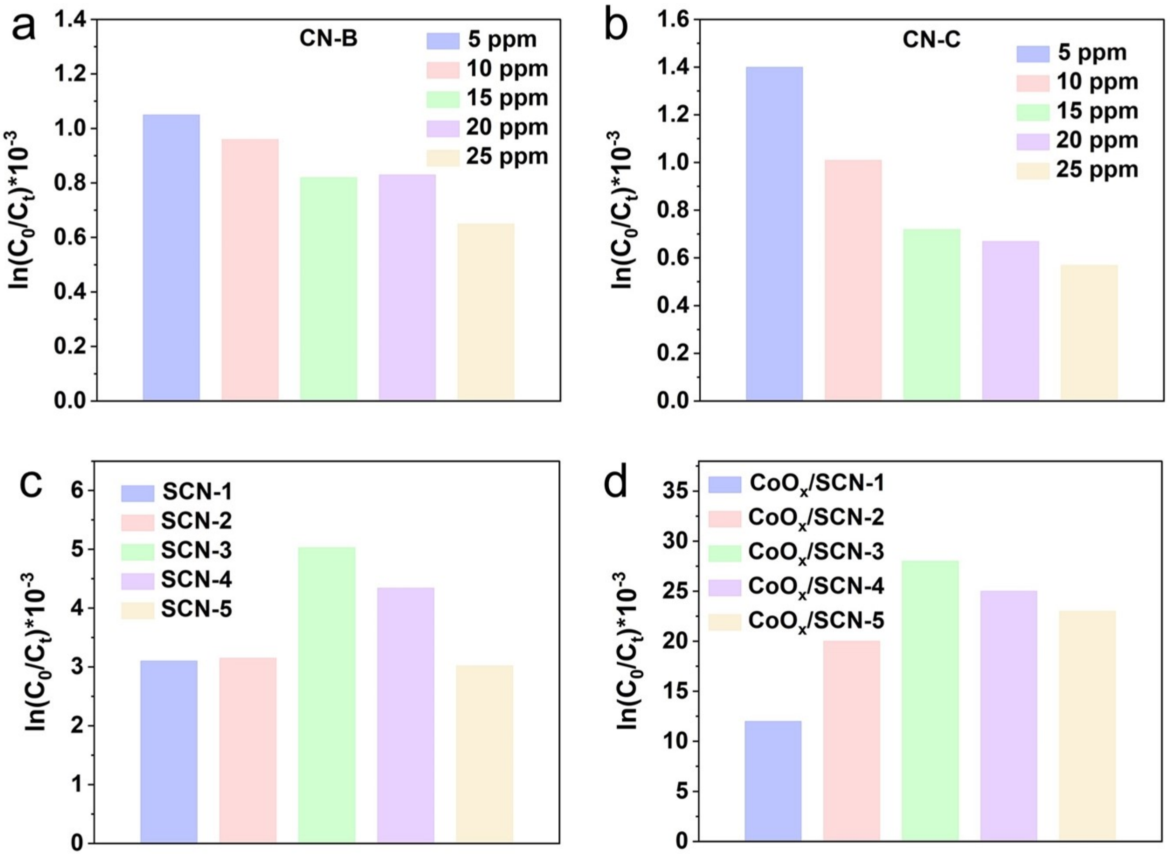

Figure S15. Reaction rate constant of (a) CN-B, (b) CN-C, (c) SCN, (d) CoO_x/SCN photocatalytic degradation of imidacloprid.

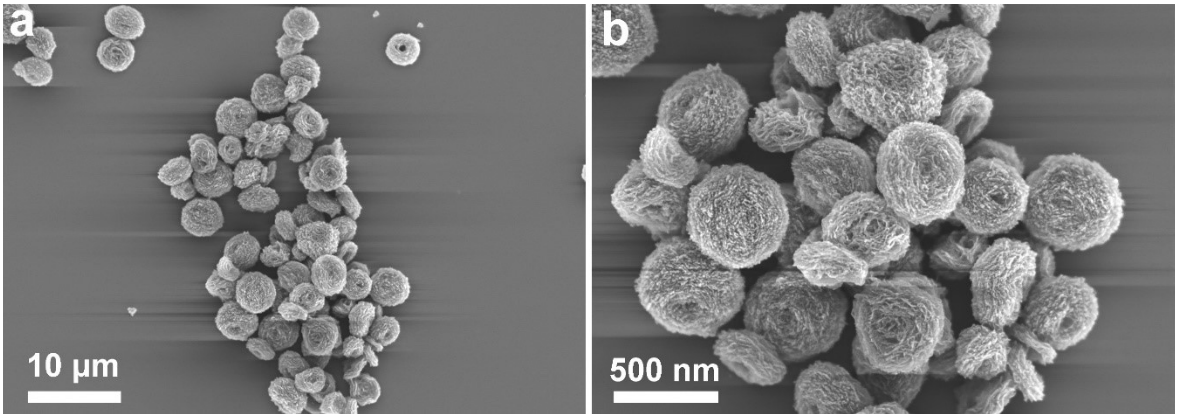

Figure S16. SEM images of CoO_x/SCN after reaction.

SEM images of the CoO_x/SCN at various magnifications reveal that its morphology remained intact after the reaction.

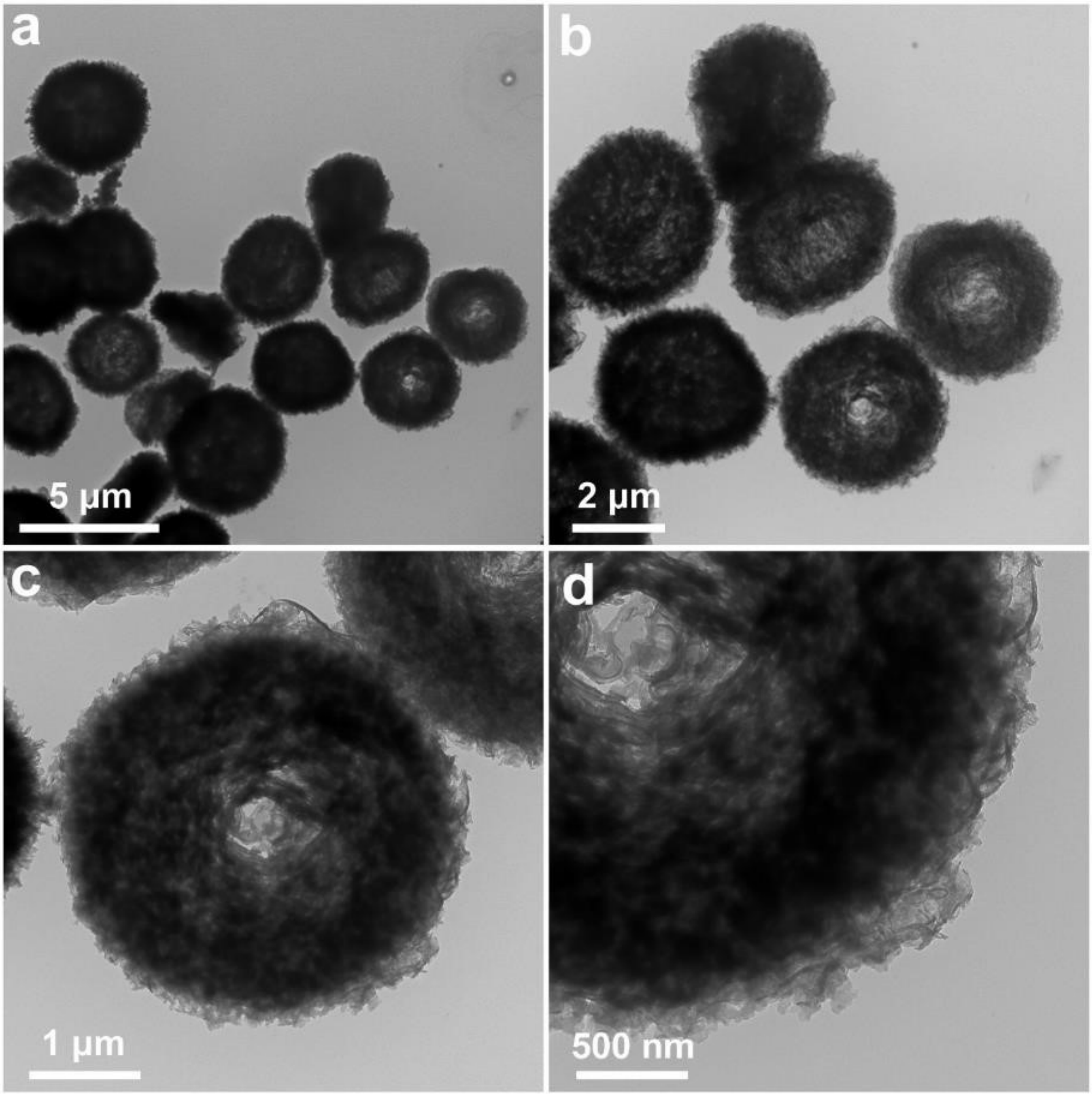

Figure S17. TEM images CoO_x/SCN after reaction.

TEM images of the CoOx/SCN at various magnifications reveal that its morphology remained intact after the reaction.

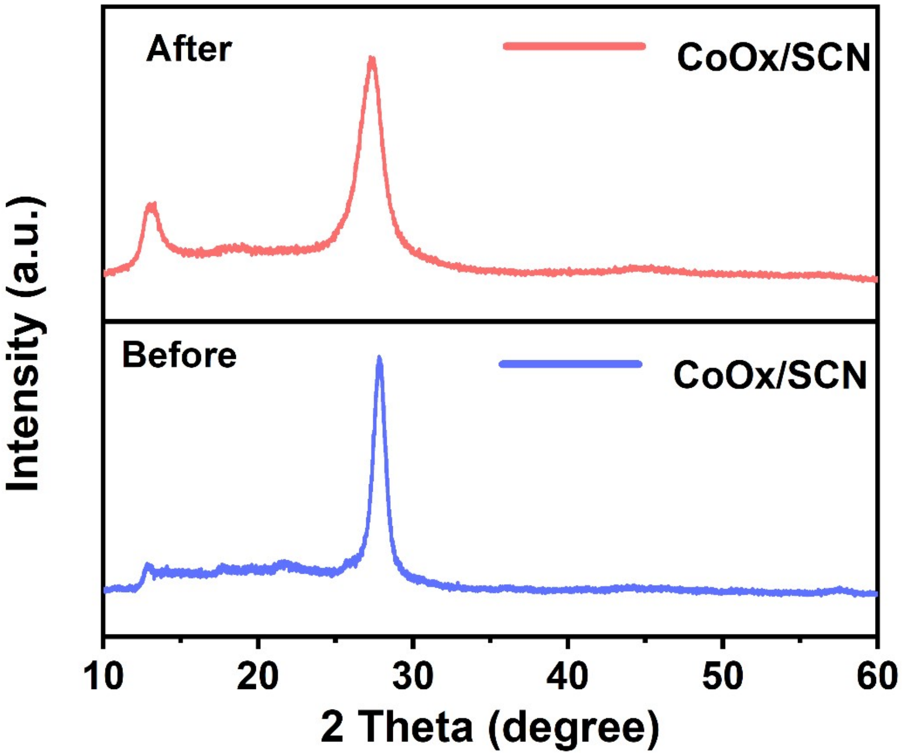

Figure S18. XRD of CoO_x/SCN before reaction and after reaction.

The XRD analysis reveals that the characteristic CN peak intensity in the CoO_x/SCN composite decreases after reaction, while its position remains unchanged. This confirms the preservation of CN's crystalline structure throughout the process. Notably, no distinct CoO_x diffraction peaks were detected in either the pre- or post-reaction samples, indicating its amorphous nature and structural stability under reaction conditions.

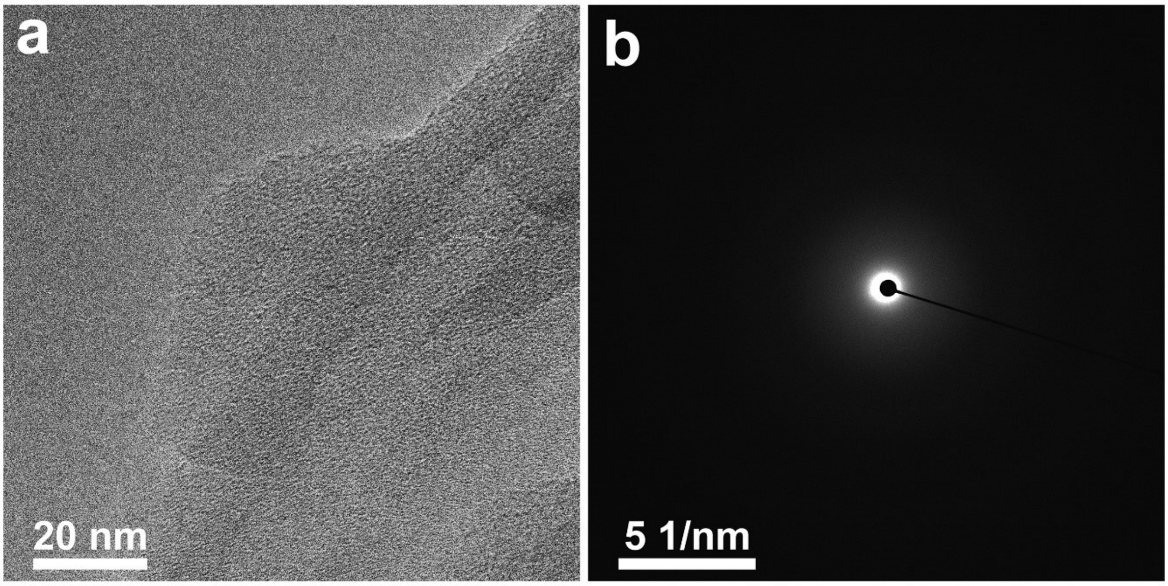

Figure S19. (a) HRTEM (b) SAED images of CoO_x/SCN after reaction.

HRTEM and SAED images of the CoO_x/SCN reveal that CoO_x remained amorphous after the reaction.

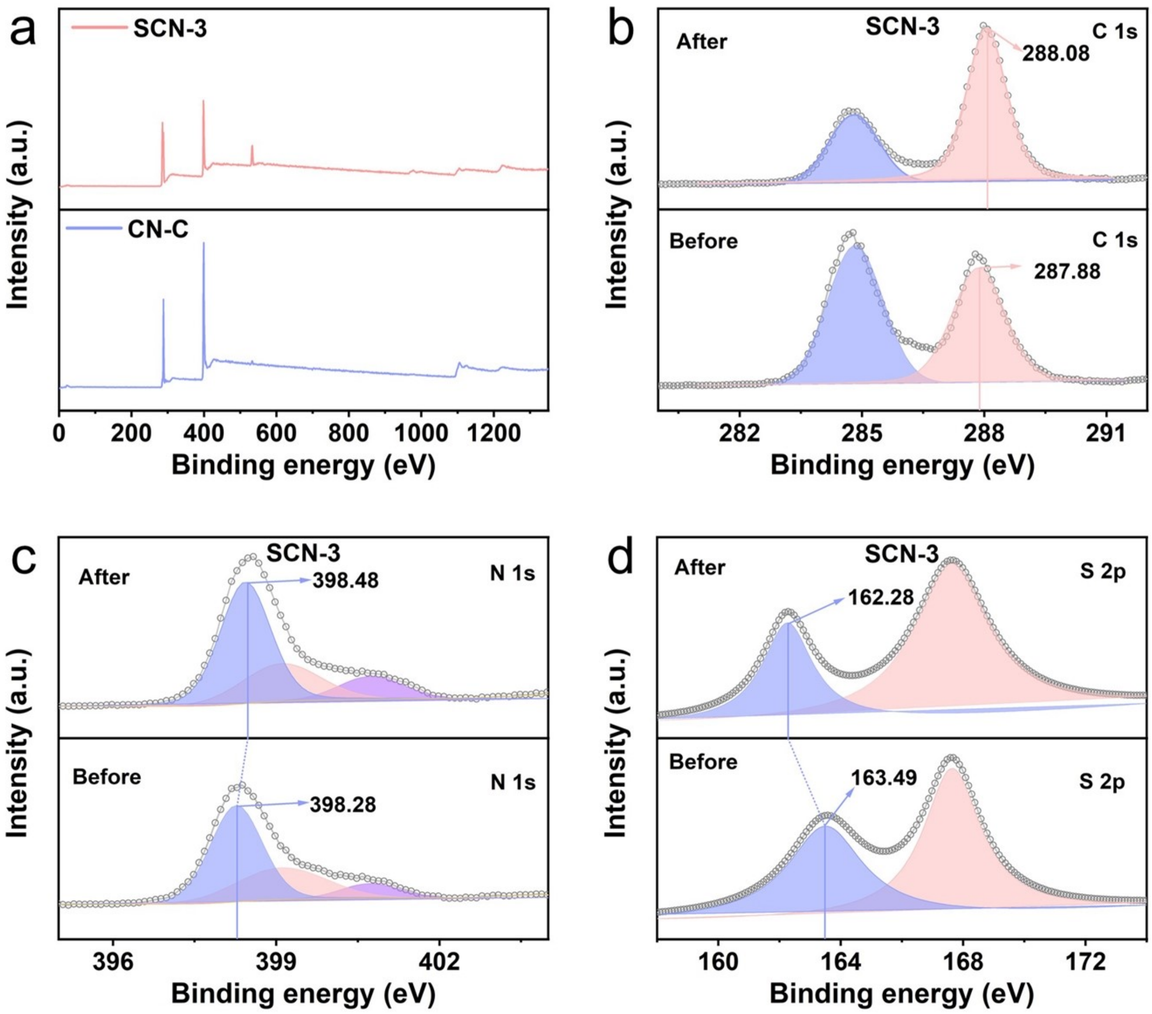

Figure S20. XPS before and after of SCN cycle.

After cycling, changes in the elemental states of SCN were observed through XPS. Specifically, the C 1s peak intensity decreased, indicating a reduction in the relative content of carbon; the N 1s peak intensity increased, reflecting a rise in the relative nitrogen content. Additionally, the S $2p_{3/2}$ peak shifted to a lower binding energy, suggesting an increase in the electronic density around the sulfur atoms and a corresponding rise in electron cloud density. These changes are likely attributed to electron transfer processes induced by photoexcitation, resulting in the sulfur atoms gaining additional electrons and undergoing a reduction in their chemical environment.

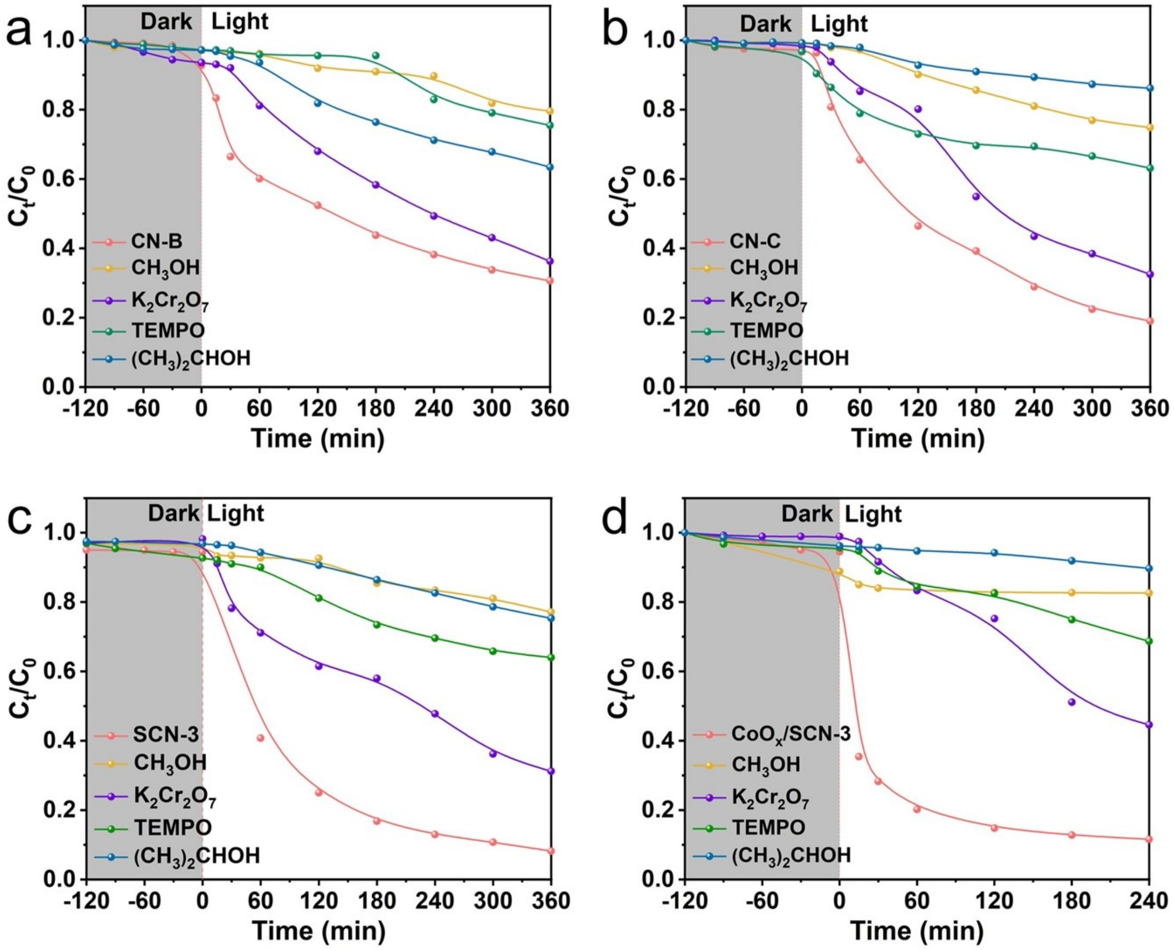

Figure S21. Photocatalytic degradation of IMI with four trappers by (a) CN-B, (b) CN-C, (c) SCN, (d) CoO$_x$/SCN.

In photocatalytic degradation experiments of IMI, four different scavengers—CH_3OH, $(CH_3)_2CHOH$, TEMPO (2, 2, 6, 6-tetramethylpiperidinyl-1-oxide), and $K_2Cr_2O_7$—were introduced to various catalyst systems. The results show that in the CN-B system, the photocatalytic degradation efficiency was relatively low with the addition of CH_3OH and TEMPO, which correspond to the trapping of holes and superoxide radicals, respectively. In contrast, for the CN-C, SCN, and CoO$_x$/SCN systems, the photocatalytic efficiency was more significantly reduced by CH_3OH and $(CH_3)_2CHOH$, corresponding to the scavenging of holes and hydroxyl radicals, respectively.

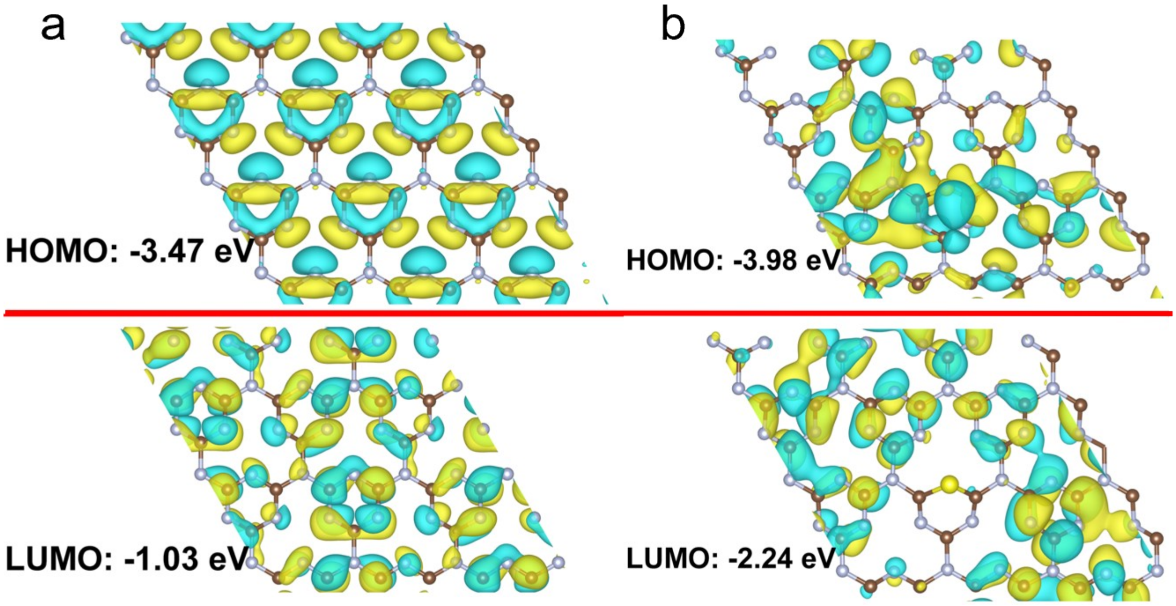

Figure S22. HOMO-LUMO gap of (a) CN-C and (b) SCN.

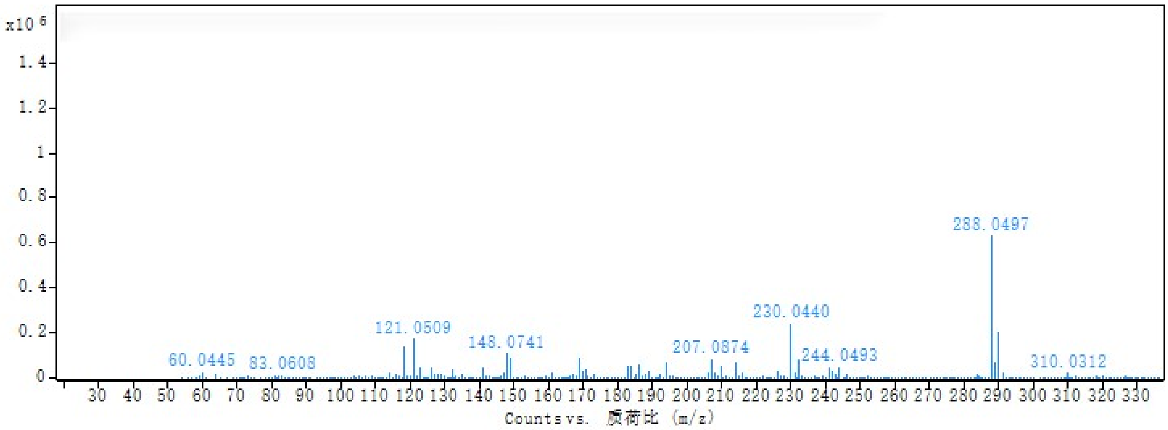

Figure S23. IMI degradation LC-MS extraction.

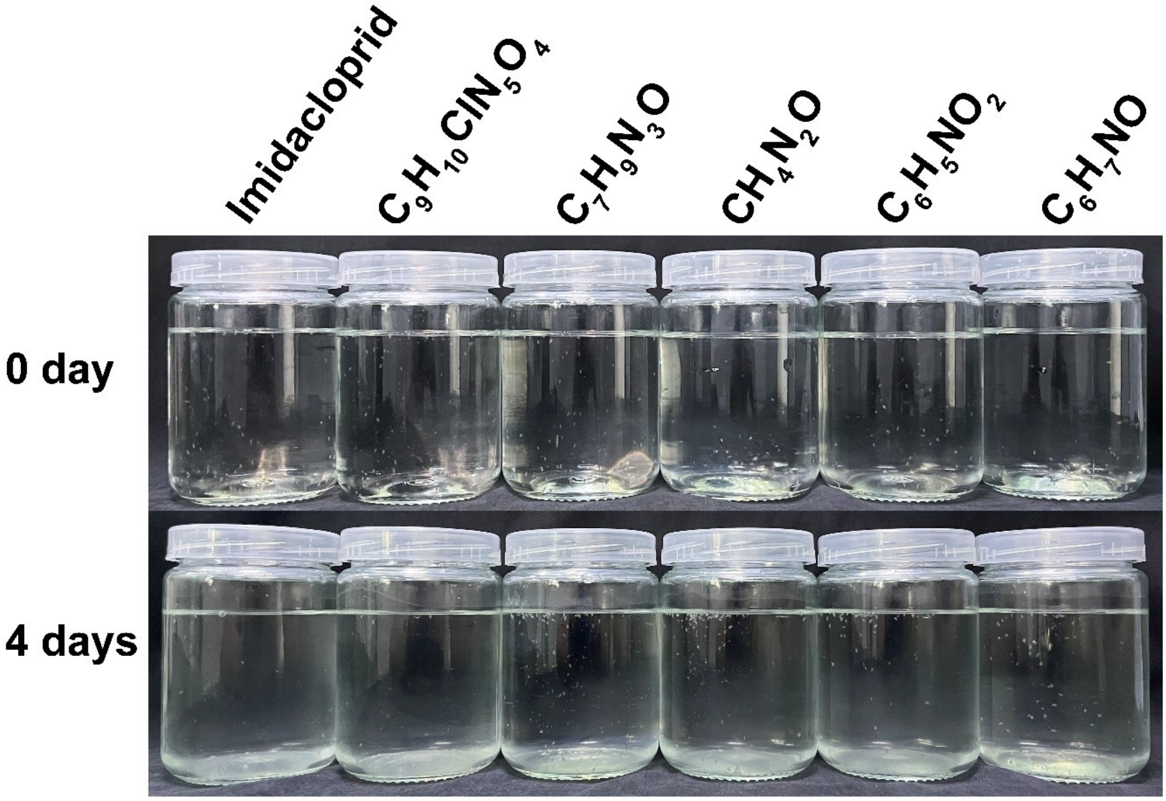

Figure S24. Safety experiment of daphnid.

The safety experiment results on water fleas show that imidacloprid is harmful to water fleas, while most of the degradation intermediates of imidacloprid are non-toxic to daphnid.

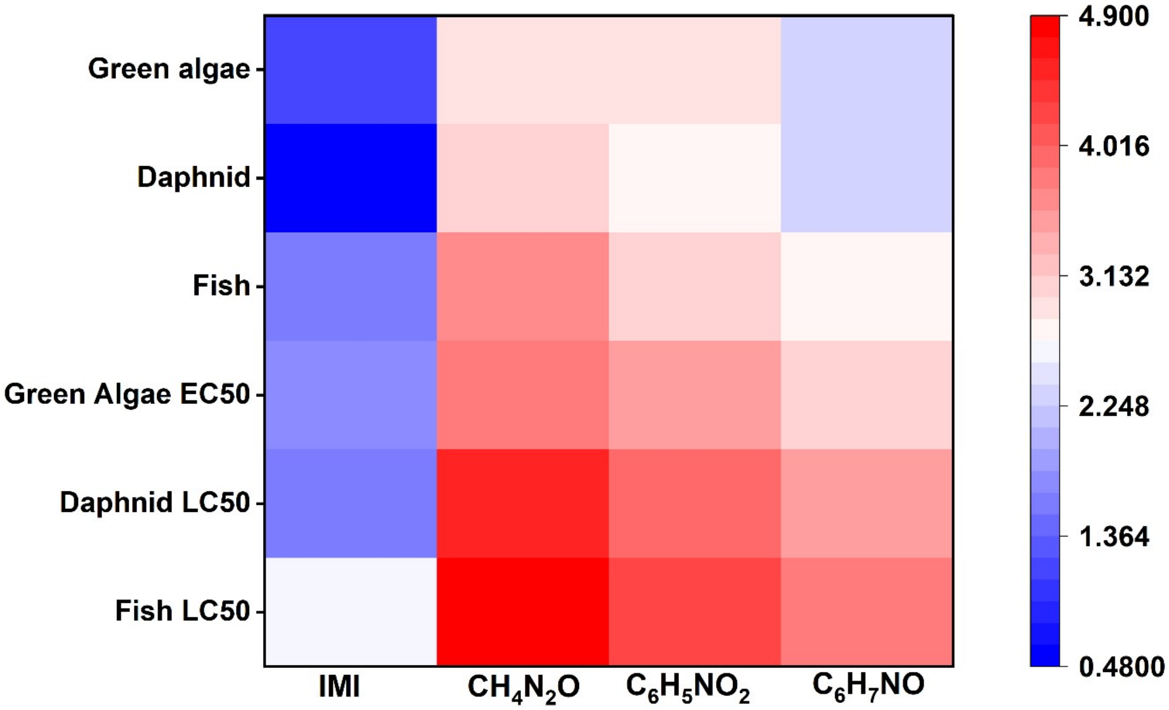

Figure S25. Calculated the chronic toxicity of imidacloprid and its removal intermediates by ECOSAR program for fish, daphnid and green algae.

Toxicity assessment reveals that while imidacloprid poses considerable environmental risks, its degradation byproducts show minimal to no toxicological impact on ecosystems.

Table S1. Comparison of the photocatalytic activity of different photocatalysts for degradation of IMI

Photocatalyst	**Light Source**	**Reaction Time (min)**	**Catalyst Quality (g/L)**	**IMI Concentration (mg/L)**	**Degradation efficiency (%)**	**Ref.**
0.5CNS/TiO_2	W lamp	150	1.0	10	93	[1]
Ag/AgBr/TiO_2	Light-emitting diode	60	1.5	10	95	[2]
Au-SnO_2-CdS	LED bulb	180	3.0	1.5	95	[3]
ZnO/$CoFe_2O_4$	Visible light	60	10	10	98	[4]
AVP/CN-0.15	Xenon lamp	240	1.0	10	38	[5]
Co_3O_4/PMS	Xe arc lamp	190	0.4	2.5	99	[6]
α-FeOOH	Fenton	3000	5	2.56	80	[7]
WO_3/CdS	Xenon lamp	30	0.5	5	80	[8]
OCN-PMS	xenon lamp	120	0.5	3	41	[9]
Fe_3O_4–Mn_3O_4	Electro-Fenton	180	2.5	60	85	[10]
CoO_x/SCN	Xenon lamp	240	0.5	5	99	**This work**

References:

[1] T. Kobkeatthawin, J. Trakulmututa, T. Amornsakchai, P. Kajitvichyanukul, S.M. Smith, *Catalysts*, 2022, **12**(2):120.

[2] J. Sun, J. Dai, R. Liu, X. Yang, *J. Chen, Res. Chem. Intermed.*, 2019, **46**, 149-164.

[3] D. Mohanta, M. Ahmaruzzaman, *Environ. Res.*, 2021, **201**, 111586.

[4] M. Naghizadeh, M.A. Taher, A.M. Tamaddon, *Heliyon*, 2019, **5**, e02870.

[5] T. Zhang, D. Zhao, Y. Wang, Y. Chang, D. Zhang, Y. Tang, X. Pu, X. Shao, *J. Am. Ceram. Soc.*, 2019, **102**, 3897-3907.

[6] R.R.M. Silva, L. Valenzuela, R. Rosal, L.A.M. Ruotolo, F.G.E. Nogueira, A. Bahamonde, *J. Environ. Chem. Eng.*, 2023, **11**(2), 109265.

[7] B. Ye, H. Cui, N. Chen, G. Fang, J. Gao, Y. Wang, *Bull Environ Contam Toxicol.*, 2023, **110**, 57.

[8] J. Li, J. Chen, Y. Ao, X. Gao, H. Che, P. Wang, *Sep. Purif. Technol.*, 2022, **281**, 119863.

[9] T. Čižmar, I. Panžić, I. Capan, A. Gajović, *Appl. Surf. Sci.*, 2021, **569**, 151026.

[10] D.D.D. Nguyen, K.A. Huynh, X.H. Nguyen, T.P. Nguyen, *Res Chem Intermed*, 2020, **46**, 4823-4840.